



Corrosion and passivation behaviour of as-cast and heat-treated AlCoCrFeNiX_{0.5} (X=Mo, Ta) high entropy alloys in 3.5 wt.% NaCl solution

Hüseyin Zengin ^{a,*}, Andreas Greul ^a, Muhammet Emre Turan ^b, Jiri Duchoslav ^c, Andrei Ionut Mardare ^{a,d}, Achim Walter Hassel ^{a,e}

^a Institute of Chemical Technology of Inorganic Materials (TIM), Johannes Kepler University Linz, Altenberger Str. 69, 4040, Linz, Austria

^b Eskipazar Vocational School, Karabük University, 78100, Karabük, Turkey

^c Center for Surface and Nanoanalytics, Johannes Kepler University Linz, Altenberger Straße 69, 4040, Linz, Austria

^d National Institute for Lasers, Plasma and Radiation Physics, 077125, Magurele, Romania

^e Danube Private University, Steiner Landstraße 124, 3500, Krems an der Donau, Austria

ARTICLE INFO

Keywords:

High entropy alloys
Microstructure
Corrosion
Passivity

ABSTRACT

In the present study, the corrosion behaviour and passivation characteristics of AlCoCrFeNi and AlCoCrFeNiX_{0.5} (X = Mo, Ta) high entropy alloys after casting and heat treatment were investigated. The alloys were produced by vacuum arc melting, followed by heat treatment at 1200°C for 5 h and rapid cooling in water. Electrochemical corrosion tests were conducted using cyclic potentiodynamic polarization and electrochemical impedance spectroscopy, focusing on corrosion resistance and passive film behaviour. The results revealed a remarkable improvement in the corrosion resistance of the base AlCoCrFeNi alloy after the heat treatment process. The as-cast Ta-containing alloy exhibited the highest pitting potential and the largest passive range among the studied alloys at room temperature. The analyses of the passive films revealed that Al oxide was the dominant oxide in passive films for all the alloys, but its porous nature negatively affected the corrosion resistance of the alloys having high fractions of Al oxide in their passive films.

1. Introduction

High entropy alloys (HEA) are multi-principal element alloys that favour the formation of solid solutions because of their high mixing entropy. Most commonly, they are defined as alloys consisting of five or more major alloying elements. This number of constituents then leads to a mixing entropy high enough to form solid solutions in most cases [1,2]. In recent years, this class of alloys has gained increasing attention because of its outstanding performance in properties like yield stress, hardness, and corrosion resistance. These advantages are thought to be caused by four “core effects”: the high entropy effect, leading to the formation of simple crystal structures such as BCC or FCC; the sluggish diffusion effect, which leads to increased high-temperature strength and stability; the severe lattice distortion effect, resulting in increased hardness; and, lastly, the cocktail effect. This effect refers to the fact that unique properties can be achieved and adjusted by mixing several components, which are not observable in any of the single elements [3]. These combined properties make HEAs excellent candidates for applications with high demands in material stability, leading to significant

research interest in fields like aerospace engineering and, of course, marine applications, which demand high stability and excellent corrosion resistance.

The alloy AlCoCrFeNi is one of the first and most extensively studied HEAs [3,4]. This alloy has gained particular attention because of its outstanding characteristics. Due to its solid solution strengthening, it shows high hardness. Furthermore, it demonstrates excellent heat stability, rendering it suitable for turbine engineering and other high-performance applications. It also shows exceptionally high corrosion resistance, mostly attributed to its Cr and Ni content [5,6]. These properties make it a perfect candidate, especially for high-demand marine applications.

Being one of the most studied HEAs and showing very promising properties, AlCoCrFeNi is a perfect candidate to explore ways of further improving the alloy’s intrinsic properties. A common approach for achieving this is to employ additional alloying elements in equiatomic or smaller quantities. There are many different elements which lead to improved properties of the alloy. The addition of Nb, for example, promotes the formation of a hypereutectic structure instead of a BCC

* Corresponding author.

E-mail address: hueseyin.zengin@jku.at (H. Zengin).

structure. Zirconium dissolves into the BCC structure and leads to an increased formation of the Laves phase [7]. Two other sensible candidates for co-alloying are Ta and Mo as valve metals exhibiting extremely stable oxides [8–10]. Tantalum has been shown to increase the solid solution strengthening and the precipitation strengthening of this alloy. Also, Ta promotes phase separation in the alloy, caused by its different mixing enthalpy, leading to these desirable changes [6]. Addition of Mo has been shown to improve the corrosion resistance of the alloy by forming a protective mixed oxide layer on the alloy's surface [7]. Furthermore, it has been indicated that already the addition of as little as 0.2 at% of Mo enhances the tensile strength and fracture elongation of the base alloy [11]. While it has been demonstrated that both of Ta and Mo are capable of improving the properties of the alloy, the scope and number of existing studies on this approach are limited. Specifically, more research on changes in corrosion properties and the influence of heat treatments after alloying is required to gain a more comprehensive understanding of this alloy system.

As discussed before, the beneficial effects of HEAs arise mostly from unique changes and processes in their lattice structure. Heat treatment is, of course, a logical step to explore further changes and adaptations for these alloys. In particular, when alloys are built from different phases, heat treatment could significantly influence the composition of these phases and therefore the overall alloy properties. While these influences are well known in the case of AlCoCrFeNi alloys, there is still a need for further exploration of these effects, particularly for the alloys with various additional alloying elements.

The expanding field of HEA research holds great potential for finding and improving materials tailored for high-demand applications. The AlCoCrFeNi, in particular, shows excellent mechanical properties and corrosion resistance. It is therefore a perfect candidate to explore different possibilities for improvement and expanding the knowledge about HEAs in general. The mechanical strength and corrosion resistance of this alloy also render it a promising candidate for marine applications, but the number of comprehensive studies exploring this possibility is limited. The aims of this paper are therefore defined based on these arguments. The corrosion resistance of the base AlCoCrFeNi was researched within the context of marine applications. The addition of Ta and Mo, as promising co-alloying elements, was explored. This was done by adding ~9 at.% of each element to the base alloy to avoid drastically altering the base properties of the alloy while potentially improving certain parameters selectively with a higher degree of control. Furthermore, possible enhancements and changes in the microstructure caused by heat treatment of the alloys were explored.

2. Experimental procedure

The equiatomic AlCoCrFeNi and AlCoCrFeNi_{0.5} (X=Mo, Ta) HEAs were fabricated by arc melting of the pure metal mixtures (>99.99 % purity) on a water-cooled Cu crucible in Ar atmosphere. The alloys are indexed based on their chemical composition and processing conditions as follows: HEA-0 represents the base AlCoCrFeNi alloy, while HEA-Mo and HEA-Ta denote modified versions containing Mo and Ta, respectively. For heat-treated samples, the suffix “(HT)” will be used. The button-shaped ingots were turned upside down and re-melted at least five times to ensure compositional homogeneity. Heat treatments were carried out at 1200°C for 5 h under argon (Ar) flow, followed by water-quenching. For microstructural analyses, the samples were first cut in half and then embedded in resin with the cross sections facing downwards. All analyses were conducted over the centre of the cross-sectional areas of the initial samples, thus eliminating possible differential effects due to dissimilar cooling rates. The embedded samples were ground using SiC grinding paper with increasing grit numbers from 220 to 4000. Then, a SiO₂ solution with a particle size of 50 nm was adopted to polish the sample surfaces, followed by cleaning with ethanol and deionised water.

The microstructures and elemental compositions of various phases in

the as-cast and heat-treated samples were investigated by Zeiss Sigma 300 Field Emission Scanning Electron Microscopy (FESEM) equipped with energy dispersive spectroscopy (EDX). The constituent phases were discovered by Rigaku Ultima IV X-ray diffractometer (XRD) at a scanning speed of 2 ° min⁻¹ and diffraction angles ranging from 10° to 90°. Microhardness tests were carried out by using QNESS Q10A+ Vickers Microhardness Tester applying a load of 1 kg (HV1) with a dwelling time of 15 s. Hardness measurements were repeated a minimum of five times on each sample.

The electrochemical measurements, including cyclic potentiodynamic polarization (CPP) and electrochemical impedance spectroscopy (EIS) were carried out by means of an Ivium Vertex potentiostat (Ivium Technologies, The Netherlands) in 3.5 wt.% NaCl solution at room temperature. A three-electrode cell setup was used for all electrochemical tests, consisting of a counter electrode (platinum (Pt) wire), a reference electrode (Ag|AgCl|3 M KCl) and a working electrode (test sample). The exposed area of the sample was 0.2 cm² and the volume of the electrolyte used in each test was 400 mL, which was purged with N₂ gas for at least 2 h beforehand to eliminate the interference of the dissolved O. Prior to all electrochemical measurements, the samples with a welded copper wire at the back were embedded in epoxy resin. Then, the surfaces were ground using SiC grinding paper with increasing grit numbers up to 4000, followed by cleaning with ethanol and deionised water. The samples were subjected to a potentiostatic reduction treatment at -0.5 V vs. SHE (standard hydrogen electrode), to remove the natural oxide film likely present on the sample surface. The reduction treatment was followed by open circuit potential (OCP) monitoring for 1 h. The CPP curves were recorded at a scan rate of 1 mV s⁻¹ starting from a voltage of -0.5 V vs. OCP. The forward scan continued until the current density reached 5 mA cm⁻², at which point the scan was reversed back to the initial potential. The EIS spectra were obtained at newly established OCP in the frequency range of 100 kHz to 0.01 Hz with a sinusoidal voltage amplitude of 10 mV rms. For each electrochemical test, a minimum of three independent measurements for each sample were performed to ensure reproducibility and reliability of the results.

The surface elemental composition of the corroded samples after immersion for 168 h was further analysed by XPS using a NEXSA G2 XPS system (Thermo Scientific, CZ) operated by the Avantage software package (Thermo Scientific, UK). The samples were examined with monochromated Al K α X-ray radiation (1486.6 eV) and a dual flood gun was utilized to compensate the built surface charge. The survey spectra were captured using a pass energy of 200 eV with an energy step of 1 eV, high-resolution spectra were acquired with a pass energy of 20 eV and an energy step of 0.05 eV.

3. Results and discussion

3.1. Microstructural characterization and hardness

The constituent phases of the HEAs in their as-cast and heat-treated conditions were characterized by XRD and the diffraction patterns are displayed in Fig. 1. The as-cast equiatomic HEA-0 alloy exhibited peaks mainly corresponding to the ordered and disordered BCC phases alongside a single peak for the FCC phase with a low intensity at around 73.7°. The heat treatment process resulted in the formation of new peaks belonging to the FCC phase at around 43.6° and 50.6°, and a slight decrease in the intensity of the BCC peaks. This indicates that the FCC phase fraction in the HEA-0 alloy showed an increase through the heat treatment process. Similar findings showing the increased FCC phase via heat treatment of AlCoCrFeNi alloy performed at comparable temperatures with those applied in this study have also been reported in previous works [4,8]. After the alloying additions of both, Mo and Ta, the primary peaks corresponding to the BCC phase were still present. Additionally, numerous peaks associated with the σ phase in the HEA-Mo alloy and the Laves phase in the HEA-Ta alloy were prominently detected. Heat

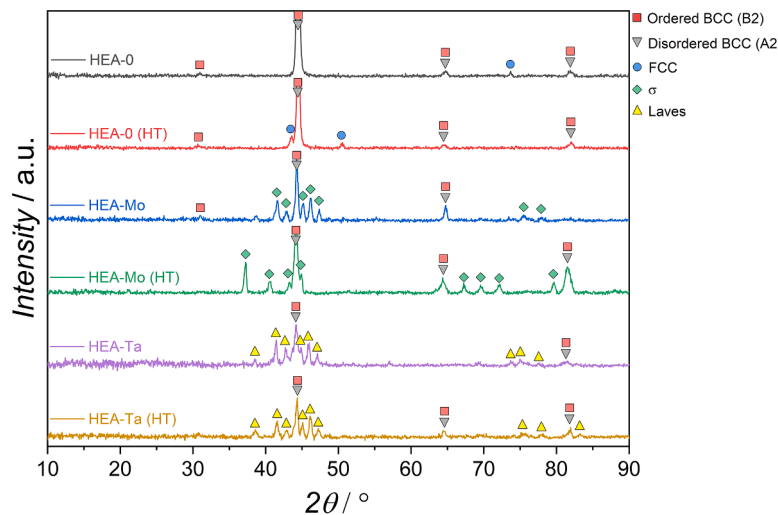


Fig. 1. XRD patterns of the as-cast and heat-treated HEAs

treatment was found to result in a slight increase in the intensity of the BCC phase in both alloys. Furthermore, while the peaks for the Laves phase in the HEA-Ta alloy remained largely unaffected following heat treatment, several σ phase peaks shifting to different positions were observed in the HEA-Mo alloy, which might be due to the partial reorientation or recrystallization of σ phases during the heat treatment process.

Fig. 2 shows the microstructures of the as-cast and heat-treated HEAs. The EDX analyses of the points indicated in the micrographs are given in Table 1. The as-cast microstructure of HEA-0 displayed typical fine dendritic morphology, consisting of dark dendrite core (DR) regions and light inter-dendritic (ID) regions. As given in Table 1, the DR region, marked as "B", contained higher Al and Ni concentrations compared to the ID region. It was reported that both, DR and ID regions in AlCoCrFeNi alloy consisted of the B2 and A2 nano-phases with various morphologies [4,6,12–14]. The differences in the concentration of elements arose from the slight variations in the relative amount of B2 and A2 phases. The DR regions exhibited a higher B2 phase content, while the ID regions were enriched in the A2 phase, relative to its

counterpart [14]. The as-cast HEA-Mo and HEA-Ta alloys also displayed dark and light regions throughout their structures, indicating the presence of two main phases in accordance with the XRD results shown in Fig. 1. According to the EDX analyses, dark regions marked as "D" and "F" for the HEA-Mo and HEA-Ta alloys, respectively, were enriched in the concentrations of Al, Ni and Co, consistent with a single BCC phase structure. The surrounding light regions in the HEA-Mo alloy exhibited significantly higher Cr and Mo concentrations, corresponding to the σ phase while those observed in the HEA-Ta alloy showed higher Cr and Ta concentrations, indicative of the Laves phase. Similar findings of these substantial compositional differences between the two phases were also observed in the AlCoCrFeNi alloy modified with Mo and Ta in the previous studies [8,15–17].

The heat treatment process led to significant alterations in the as-cast microstructure of all HEAs, as seen in Fig. 2 (d-f). This primarily resulted from the transition from non-equilibrium states to equilibrium states during high-temperature heat treatment, where significant atomic diffusion occurs, influencing various reaction processes such as precipitation and/or dissolution of phases. In general, the fine dendritic as-cast

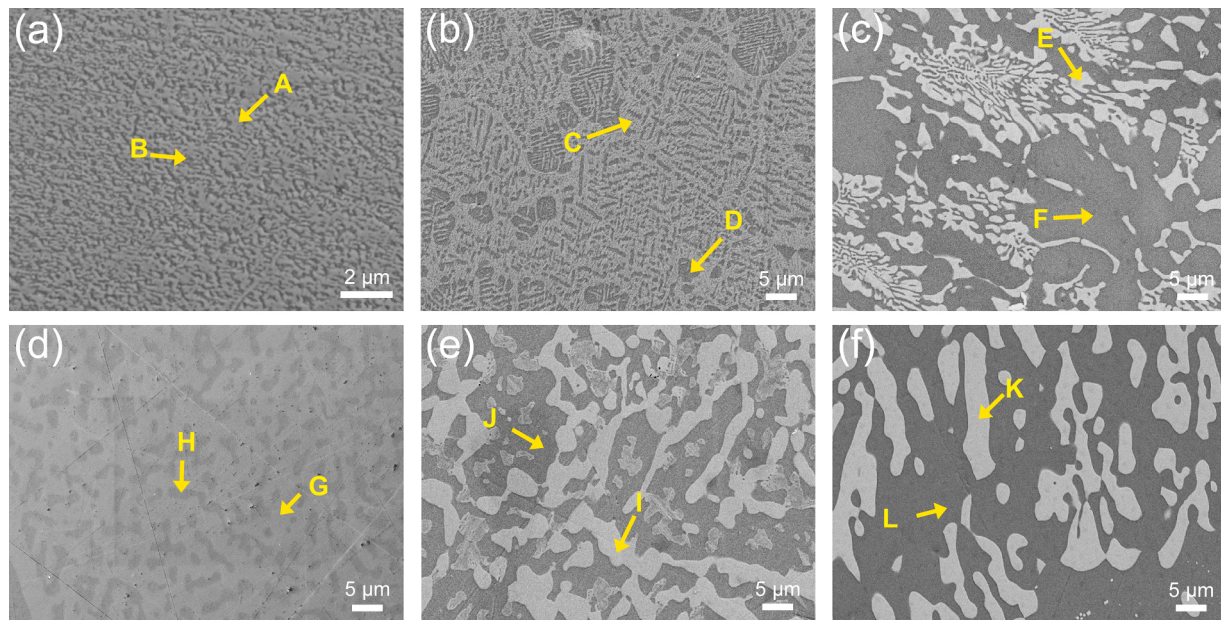


Fig. 2. SEM micrographs of the (a-c) as-cast and (d-f) heat-treated HEAs: (a,d) HEA-0, (b,e) HEA-Mo and (c,f) HEA-Ta samples

Table 1

EDX results of the points indicated in Fig. 2

Condition	Sample	Point	Elements / at.%						
			Al	Co	Cr	Fe	Ni	Mo	Ta
As-cast	HEA-0	A	17.9	19.4	22.4	21.7	18.6	–	–
		B	22.5	19.5	18.3	18.2	21.5	–	–
	HEA-Mo	C	13.4	17.0	22.9	19.8	10.6	16.3	–
		D	22.3	21.1	13.2	15.2	24.6	3.6	–
	HEA-Ta	E	10.5	17.2	23.6	19.2	10.7	–	18.8
		F	26.1	18.3	11.2	18.1	24.2	–	2.1
Heat-treated	HEA-0	G	13.5	17.7	28.3	23.6	16.9	–	–
		H	26.4	18.0	12.6	14.4	28.6	–	–
	HEA-Mo	I	9.5	16.1	26.3	20.4	8.4	19.3	–
		J	26.4	20.1	11.3	13.7	27.3	1.2	–
	HEA-Ta	K	7.2	19.9	27.1	17.4	7.8	–	20.6
		L	29.2	15.3	8.5	17.6	28.4	–	1.0

structures of HEAs, resulting from the high-temperature gradient imposed by the water-cooled mould, transformed into a significantly coarser microstructure through heat treatments. According to XRD results, an increase in the FCC phase fraction was observed in the HEA-0 alloy after the heat treatment. Furthermore, it was reported elsewhere that the precipitation of the FCC phase mostly occurred along the grain boundaries during heat treatment [4,18]. However, their fine structures could not be exposed in SEM analyses. The EDX results revealed a notable increase in Al and Ni concentrations within the dark regions, while slight increases in Cr and Fe concentrations were observed in the light regions as a result of the heat treatment. For the HEA-Mo and HEA-Ta alloys, heat treatments resulted in further increases in the Mo and Ta concentrations, respectively, within the light regions, together with even lower Al concentrations. On the other hand, similar to HEA-0 alloy, the Al and Ni concentrations in the dark regions also showed a considerable increase. The net-like in the cast HEA-Mo microstructure turned into a much coarser form after heat treatment.

The Vickers hardness values of the as-cast and heat-treated HEAs are summarized in Fig. 3. The HEA-0 alloy showed the lowest hardness values among the studied alloys. The addition of Mo and Ta gave rise to significant increases in the hardness of both, as-cast and heat-treated samples, where the HEA-Ta alloy showed slightly higher hardness than the HEA-Mo alloy. It is known that the FCC phase has a lower hardness than the BCC phase in HEAs [19,20]. The increased proportion of FCC phase in the HEA-0 (HT) alloy would normally lead to a decrease in the hardness of this alloy. However, the heat treatment resulted in an increase in the hardness of the HEA-0 alloy by 38.6 HV. This can be explained by the assumption that the low amount of fine-structured precipitation of the FCC phase did not lead to a reduction in the

hardness noticeably and the spinodal decomposition and more homogeneous microstructure induced through the heat treatment improved the hardness of HEA-0 alloy to a certain extent. Furthermore, the significant improvements in the hardness values obtained by the addition of Mo and Ta were mainly due to the severe lattice distortion and the high amount of hard and brittle σ phase in the HEA-Mo alloy and Laves phase in the HEA-Ta alloy [8,17].

3.2. Corrosion behaviour

Fig. 4 shows the open circuit potential (OCP) measurements up to 1 h in 3.5 wt.% NaCl solution and cyclic potentiodynamic polarization (CPP) curves obtained for the as-cast and heat-treated HEAs. All samples showed relatively stable OCP values as the immersion time reached around 10 min. The as-cast HEA-0 displayed the highest OCP during the entire immersion period, whereas the heat treatment process led to slight decreases in its values, while still being higher than those of both, as-cast and heat-treated HEA-Mo and HEA-Ta alloys. The heat treatment did not similarly affect the HEA-Mo and HEA-Ta alloys. For instance, the as-cast HEA-Mo alloy exhibited much lower OCP values at all immersion times compared to those for the HEA-Mo (HT) alloys. Furthermore, the OCP values for the HEA-Ta (HT) alloy were higher than its as-cast counterpart up to 15 min. Afterwards, they gradually decreased until the end of the immersion period, eventually showing the lowest OCP values among the studied alloys. Although OCP monitoring can provide insights into the thermodynamics of an electrochemical system, the obtained OCP values do not directly characterise kinetic aspects and thereby no direct correlation between the OCP values and overall corrosion can be found [21]. Accordingly, while the low OCP values observed for HEA-0 alloy suggest a potentially reduced thermodynamic tendency towards corrosion compared to other alloys, further results revealed that the actual corrosion behaviour was significantly influenced by additional factors, providing a more comprehensive understanding of both thermodynamic and kinetic aspects.

The CPP curves, shown in Fig. 4(b-d) were performed to gain a better understanding of the corrosion kinetics and repassivation capabilities of the studied HEAs. The derived parameters of corrosion potential (E_{corr}), corrosion current density (i_{corr}), primary passivation potential (E_{pp}), passivation current density (i_{pass}), repassivation potential (E_{rp}), breakdown potential (E_{bd}) and passive region range (ΔE) are given in Table 2. Since most of the polarisation curves do not have a clear active-passive transition peaks, E_{pp} values were determined from the intersection point between the active region and a linear interpolation from the initial passivation area following the active region of the polarisation curve. This approach is intended to provide a consistent and reproducible way of determining E_{pp} values for all samples.

The hysteresis observed in the CPP curves provides valuable information, especially about the self-healing ability of the passive films of the alloys. Negative hysteresis occurs when the current density during

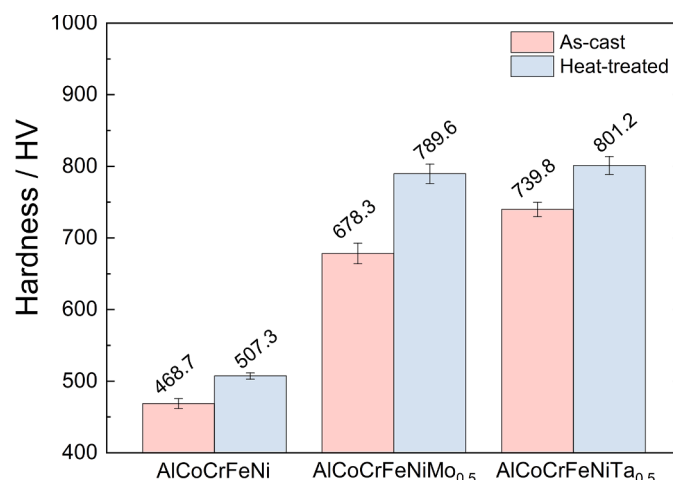


Fig. 3. Vickers hardness values of the as-cast and heat-treated HEAs

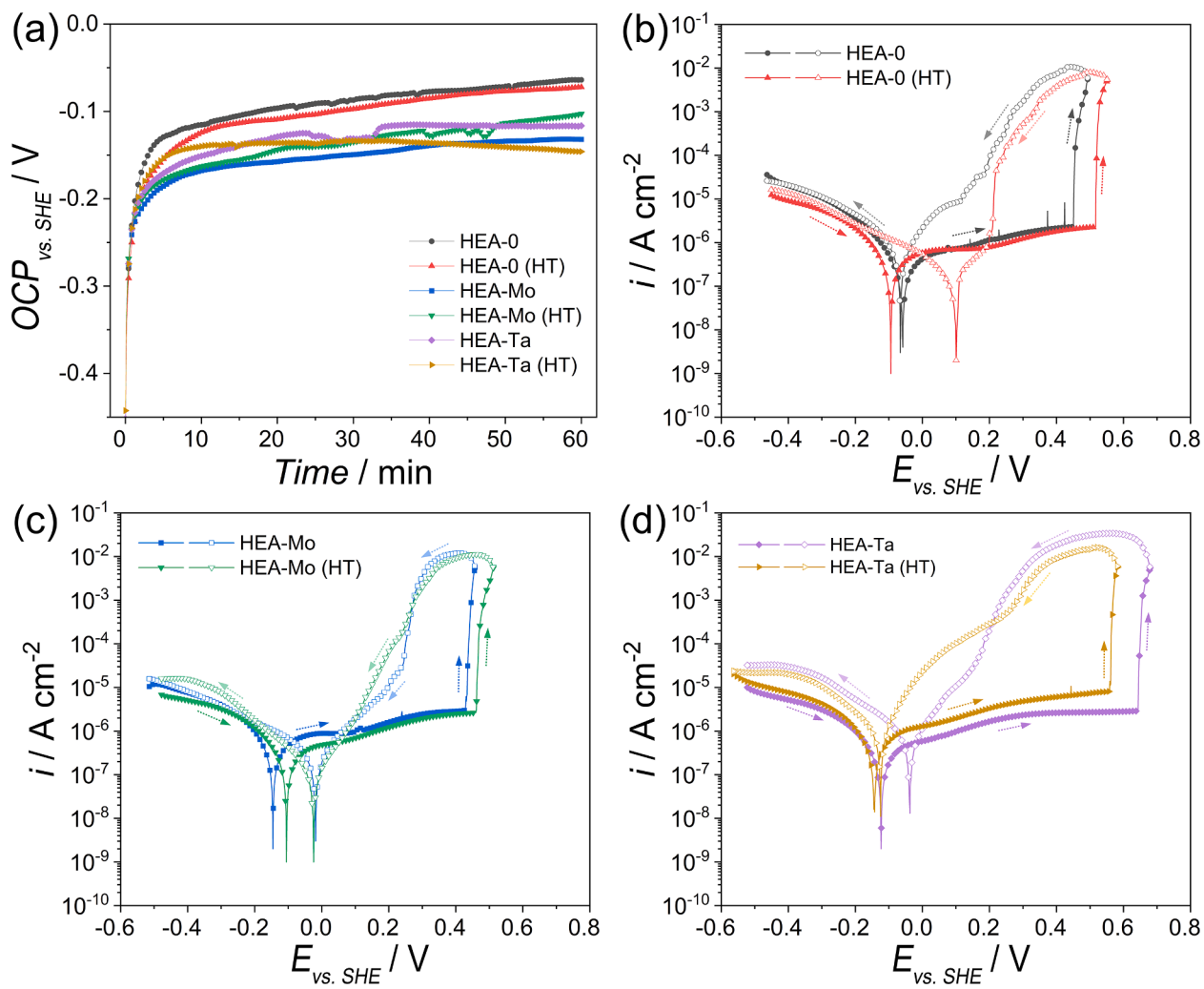


Fig. 4. (a) Open circuit potential values and (b-d) cyclic potentiodynamic polarization curves of as-cast and heat-treated (b) HEA-0, (c) HEA-Mo and (d) HEA-Ta samples

Table 2

Parameters derived from polarization curves in Fig. 4

Condition	Sample	E_{corr}/mV	$i_{corr}/\mu A \cdot cm^{-2}$	E_{pp}/mV	$i_{pass}/\mu A \cdot cm^{-2}$	E_{rp}/mV	E_{bd}/mV	$\Delta E (E_{bd} - E_{pp})/mV$
As-cast	HEA-0	-58 ± 2.2	0.28 ± 0.05	56 ± 2.5	0.63 ± 0.07	-64 ± 2.8	448 ± 2.1	392
	HEA-Mo	-146 ± 2.9	0.33 ± 0.03	-14 ± 1.9	0.87 ± 0.07	54 ± 2.5	428 ± 2.6	442
	HEA-Ta	-123 ± 3.2	0.26 ± 0.05	-11 ± 2.1	0.48 ± 0.05	-18 ± 2.1	644 ± 2.5	655
Heat-treated	HEA-0	-95 ± 1.8	0.25 ± 0.04	18 ± 2.3	0.65 ± 0.08	190 ± 3.0	517 ± 1.9	499
	HEA-Mo	-105 ± 2.0	0.23 ± 0.03	-29 ± 1.8	0.42 ± 0.07	52 ± 2.8	460 ± 2.5	489
	HEA-Ta	-144 ± 2.7	0.50 ± 0.06	-50 ± 2.6	1.03 ± 0.09	-117 ± 2.5	558 ± 2.8	608

the reverse scan is lower than that during the forward scan. However, as illustrated in Fig. 4(b-d), in the CPP curves of all the alloys, the current densities of the reverse scans were higher than those of the forward scans, which created positive hysteresis [22]. This indicates that pitting corrosion occurred in all the alloys and the pits were not able to repassivate themselves readily. In addition, a larger loop area of the positive hysteresis can be an indication of the continual growth of the nucleated pits on the surface and weak repassivation capability. Among the studied alloys, HEA-0 (HT), HEA-Mo and HEA-Mo (HT) alloys displayed relatively smaller hysteresis loop and more positive E_{rp} values, compared to the other alloys, meaning that their repassivation capabilities were improved. The enhancement of the repassivating properties particularly induced by Mo addition into various alloys has long been investigated in numerous studies [23–26]. It is generally accepted that

Mo redeposits upon dissolution and provides favourable synergetic effects with Cr in the oxide film.

The as-cast HEA-0 was the only alloy that displayed an E_{rp} value lower than the respective E_{corr} , which was an indication of poor repassivation. The HEA-0 alloy also had the lowest passive range (392 mV) and displayed considerable metastable pitting in its passive region. The heat treatment process resulted in significant improvements particularly in the E_{rp} , E_{bd} and ΔE values of the HEA-0 alloy, together with a slight reduction in the i_{corr} values. Additionally, the HEA-0 (HT) alloy did not show any metastable pitting in its passive region. Gu et al. also reported that the passivation characteristics of AlCoCrFeNi alloy were remarkably improved after a heat treatment process at 1100 °C, which was mainly attributed to the increased amount of FCC phases and lack of intermetallic phases [4]. Principally, the corrosion resistance of

equiatomic AlCoCrFeNi alloy is deeply influenced by the amount and morphology of the DR and ID regions and other possible phases in the structure. Corrosion initiation is more prone in DR regions compared to ID regions. In addition, the B2 ordered phase, which is rich in Al and Ni but poor in Cr, extremely deteriorates pitting corrosion resistance and weakens the repassivation ability [4,27,28]. Therefore, the significant improvement in the passivation characteristics of the as-cast HEA-0 alloy by heat treatment can be primarily attributed to the increased FCC phase, which partially replaced the B2 ordered phase.

The corrosion behaviour of the HEA-Mo alloy improved slightly after heat treatment, though not as much as that of the HEA-0 alloy. All derived parameters, as given in Table 2, showed enhancements through heat treatment. Even the few instances of metastable pitting behaviour observed in the passive region of HEA-Mo alloy were completely eliminated after heat treatment. It is also worth noting that the HEA-Mo (HT) alloy showed the lowest i_{corr} and i_{pass} values among all the alloys investigated, indicating higher stability of the passive film. The reduced current density of the passive film induced by Mo addition was likely due to the presence of Mo species in the passive layer, such as $\text{MoO}(\text{OH})_2$ or MoO_4^{2-} , which are adsorbed at the surface, acting as barriers against corrosion attacks [24,29–31]. Furthermore, as the MoO_4^{2-} ions were present in the outer regions of the surface film, it could potentially enhance the formation of Cr oxide in the inner regions [25,32]. However, as previously mentioned, the as-cast and heat-treated HEA-Mo alloys exhibited significant variations in their phase concentrations, particularly for Al, Ni, Cr and Mo. As shown in Table 1, the σ phase in light regions displayed much higher Mo and Cr concentrations than those in the BCC phase in the dark regions, which were significantly enriched in Al and Ni. Heat treatment led to increases in the concentrations of Mo and Cr in the σ phase and similarly Al and Ni in the BCC phase. However, no depletion of Cr was observed in the BCC phase upon heat treatment as its concentration remained almost constant. Thus, the synergistic effects of Mo and Cr continued and were even more pronounced after heat treatment. The change in the phase morphologies might have also played a role in changes in the corrosion properties of the HEA-Mo alloy. The net-like structure of the phases in the as-cast HEA-Mo alloy transformed into a much coarser form after heat treatment. It has been reported that galvanic couplings could occur between the BCC and σ phases due to the significant variations in Cr and Mo, where the Cr and Mo-rich σ phase might act as a cathode [33,34]. Therefore, the high cathode/anode surface area in the structure of the as-cast HEA-Mo alloy may have caused more galvanic interaction and this effect ceased with decreasing this area after heat treatment, resulting in reduced corrosion rates.

The employment of Ta appeared to have unique effects on the corrosion behaviour of the AlCoCrFeNi alloys. As can be seen in Fig. 4(d) and Table 2, the as-cast HEA-Ta alloy exhibited by far the largest E_{bd} and ΔE values. Furthermore, no evidence of metastable pitting was observed in the passive region of the HEA-Ta alloy. Besides, the i_{corr} and i_{pass} values were the second lowest among the studied alloys. These findings indicate that the addition of Ta could effectively improve the corrosion resistance and passivation characteristics of the as-cast AlCoCrFeNi alloy. However, the E_{rp} values for the as-cast and heat-treated HEA-Ta alloy were found to be poor compared to those for the other samples, suggesting that Ta addition had no effect in improving the repassivation ability of AlCoCrFeNi alloy. One of the few investigations reported in the literature, exploring the effects of Ta addition on the corrosion behaviour of AlCoCrFeNi alloys also reported that Ta additions up to ~5.7 at.% considerably enhanced the corrosion resistance and passivation characteristics of AlCoCrFeNi alloy [17]. The increasing Ta content mostly facilitated the formation of stable Ta_2O_5 , which played the main role in the corrosion improvement. The same study also suggested the presence of microgalvanic coupling between the Laves phase and the BCC phase. As shown in Fig. 2(c), the fine dispersion of the island-like Laves phases, enriched in Cr and Ta, contributed to the formation of

Ta-based oxides and protected the sample from pitting formation effectively. However, the HEA-Ta was the only alloy for which heat treatment affected the corrosion rate adversely, among the studied alloys. As given in Table 2, the highest i_{corr} and i_{pass} values were found for the HEA-Ta (HT) alloy. Nevertheless, the general passivation resistance displayed improvements, as evidenced by the remarkably high E_{bd} and ΔE values, which were comparable to those of the as-cast HEA-Ta alloy. This behaviour can be mainly attributed to the microstructural variations as a result of the heat treatment. For example, the BCC phase fraction increased in the HEA-Ta alloy upon heat treatment, which is known to facilitate preferential corrosion initiation [17,20]. Moreover, as shown in Fig. 2 and Table 1, the Cr and Co concentrations of the BCC phase (dark regions) in the HEA-Ta alloy decreased after heat treatment, while a further enrichment of Cr and Ta in the Laves phase was observed. This suggests that microgalvanic interaction between the phases may have dominated the corrosion mechanism in the HEA-Ta (HT) alloy, thus increasing the corrosion rate. Yet, the protective effect of Ta-based oxides evidently persisted, keeping the passive range stable up to a certain level. It should also be noted that a transient current fluctuation was observed within the passive region of the HEA-Ta (HT) alloy, suggesting the occurrence of metastable pitting. This indicates a marginal increase in the localized corrosion tendency of the HEA-Ta alloy following heat treatment.

The EIS spectra obtained for the as-cast and heat-treated HEAs in 3.5 wt.% NaCl solution, following reduction treatment and OCP monitoring for 1 h are illustrated in Fig. 5. The Nyquist plots exhibited incomplete capacitive semicircular arcs, with centres depressed below x-axis, suggesting one time constant predominantly controlled by the charge transfer process at the electrode/solution interface [29,35]. The arc diameters in the Nyquist plots varied depending on the alloy composition and heat treatment. Among the studied alloys, the as-cast HEA-0 and HEA-Mo alloys, as well as the heat-treated HEA-Ta (HT) alloy, displayed relatively small arcs, while the rest had comparably larger curves, indicating increased charge transfer resistance. The EIS spectra were fitted to obtain impedance data using the equivalent circuit shown in Fig. 6, where R_s represents the electrolyte resistance, R_1 denotes the polarization resistance, encompassing both charge transfer and passive film behaviours, and CPE₁ corresponds to the double-layer capacitance. Based on the EIS parameters, the effective capacitance, C_{eff} , values and corresponding passive film thicknesses were also calculated. The derived parameters are given in Table 3. For the calculation of C_{eff} , the power-law model was used, which is independent of the characteristic frequency and extracts the information from the high-frequency part of the EIS spectra, using the following equation [36–38]:

$$C_{eff} = gQ(\rho_\delta \epsilon \epsilon_0)^{1-n}$$

where g is a function of n , which can be calculated using the formula; $g = 1 + 2.88(1 - n)^{2.375}$, Q is the parameter of CPE elements, ϵ is the relative permittivity number of the passive film (15.6 for HEAs [39]) and ϵ_0 is the vacuum permittivity ($8.8542 \times 10^{-14} \text{ F cm}^{-1}$). According to the adopted power-law distribution of resistivity, ρ_δ represents the boundary value of resistivity at the interface. A value of $\rho_\delta = 500 \Omega \text{ cm}$ was chosen based on literature, specifically as discussed by Orazem et al. [36], who found this value consistent with the semiconducting properties of oxide films on X12CrNiMoV12-3 martensitic steels and 18Cr-8Ni (303 stainless steel). Hirschorn et al. [37] reported $\rho_\delta = 450 \Omega \text{ cm}$ for Fe17Cr stainless steel using impedance data and XPS measurements, which Orazem et al. [36] rounded to $\rho_\delta = 500 \Omega \text{ cm}$ to account for uncertainties in oxide thickness measurements, dielectric constant assumptions and film homogeneity. Despite potential variations due to alloy composition differences, this fixed value was adopted for consistency. Furthermore, the thickness of the passive film (δ) was calculated by the following equation:

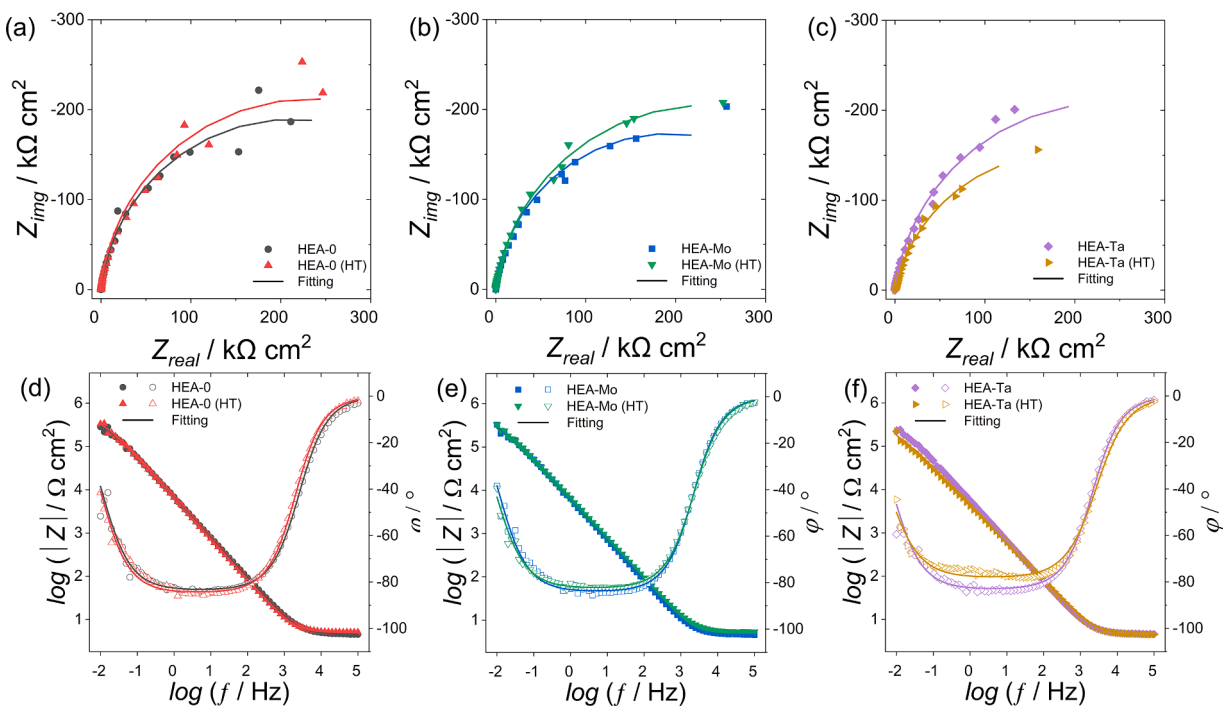


Fig. 5. EIS spectra of the as-cast and heat-treated (a,d) HEA-0, (b,e) HEA-Mo and (c,f) HEA-Ta samples

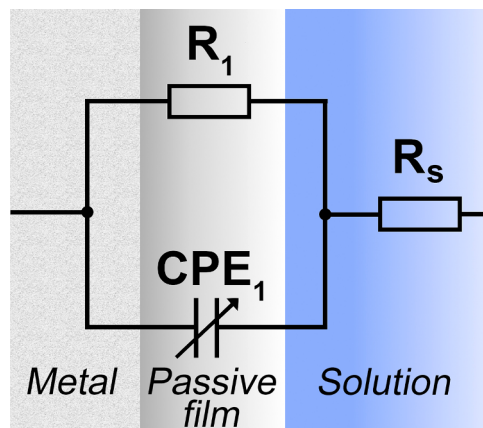


Fig. 6. Equivalent circuit used for fitting EIS spectra

$$\delta = \frac{\epsilon \epsilon_0}{C_{eff}}$$

The derived data presented in Table 3 indicates that the capacitance of the film on the surface of HEA-0 alloy displayed only a marginal increase after heat treatment and accordingly minimal variations in the passive film thickness values were observed. However, the polarization resistance of the HEA-0 (HT) alloy was much higher than the as-cast HEA-0 alloy, demonstrating that the heat treatment efficiently

enhanced the protectiveness of the surface, independent of the effect of the oxide thickness. For the as-cast HEA-Mo alloy, both polarization resistance and capacitance values were lower than those of the base HEA-0 alloy. Besides, there were no significant changes in the calculated capacitance or film thickness values after heat treatment. Nevertheless, the substantial increase in the polarization resistance following heat treatment indicated a noticeable improvement in the corrosion resistance of the HEA-Mo alloy. Moreover, the as-cast HEA-Ta alloy showed the highest polarization resistance among the studied alloys, whereas the lowest polarization resistance and the lowest capacitance values were obtained for the HEA-Ta (HT) alloy. Overall, the EIS results coincided well with the potentiodynamic test results. The noticeably high calculated film thickness and the low polarization resistance of the HEA-Ta (HT) alloy can potentially be attributed to the formation of a film with a more porous nature and/or non-uniform structure and density [25,40].

The passive films of HEAs, following polarization at 200 mV vs. SHE for 1 h in 3.5 wt.% NaCl solution, were further analysed using XPS, and the obtained spectra of O1s, Al2s, Co2p, Cr2p, Fe2p, Ni2p, Mo3d and Ta4d are shown in Fig. 7. The O1s spectra were deconvoluted by OH⁻ peak at ~532 eV, signifying the presence of metal hydroxides together with potential organic groups that may have resulted from the potential residues transmitted during surface preparation and O²⁻ peak at ~530 eV, which belonged to all oxidic structures in the passive film. The most notable observation when comparing the O²⁻ peaks was that the peak intensity for the as-cast HEA-Ta alloy was higher than those for the other alloys, suggesting that the relative amount of oxides in the passive film of HEA-Ta alloy was the highest. This could be advantageous,

Table 3
Equivalent circuit parameters derived from EIS data fitting

Condition	Sample	$R_s/\Omega \cdot \text{cm}^2$	$CPE_1/\Omega^{-1} \cdot \text{s}^n \cdot \text{cm}^{-2}$	n_1	$R_1/\text{k}\Omega \cdot \text{cm}^2$	$C_{eff}/\mu\text{F} \cdot \text{cm}^{-2}$	δ/nm
As-cast	HEA-0	4.64	2.72×10^{-5}	0.93	425.9	6.24	2.21
	HEA-Mo	4.66	2.96×10^{-5}	0.93	386.3	5.51	2.5
	HEA-Ta	4.63	3.35×10^{-5}	0.92	470.1	6.24	2.21
Heat-treated	HEA-0	5.07	2.74×10^{-5}	0.94	467.8	6.29	2.20
	HEA-Mo	5.36	2.91×10^{-5}	0.92	468.6	5.42	2.55
	HEA-Ta	4.36	4.81×10^{-5}	0.87	375.0	3.17	4.36

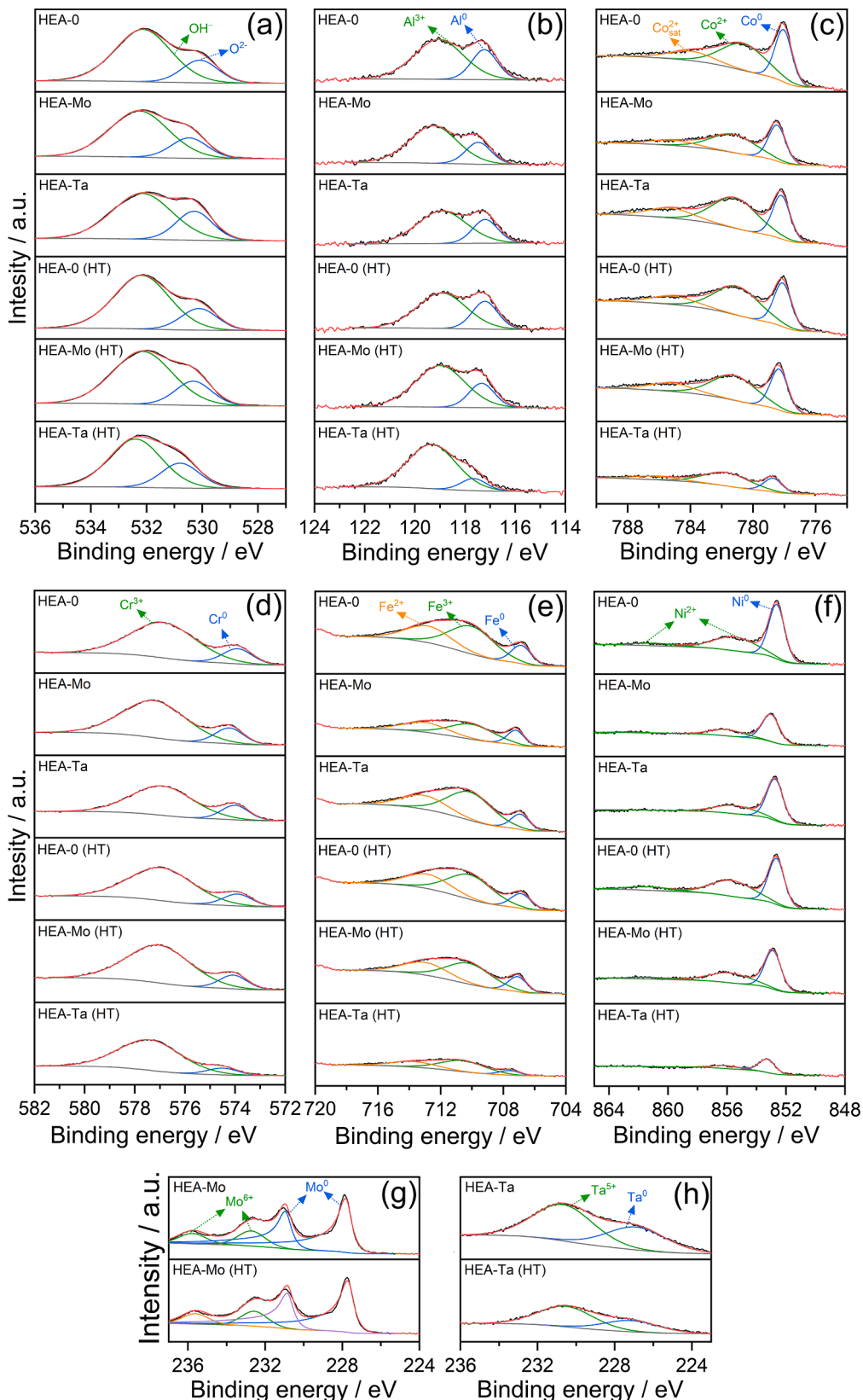


Fig. 7. XPS spectra obtained on the passive films of HEAs: (a) O1s, (b) Al2s, (c) Co2p, (d) Cr2p, (e) Fe2p, (f) Ni2p, (g) Mo3d and (h) Ta4d

particularly for the pitting corrosion resistance since hydrogen-containing species can accelerate pitting corrosion due to the incorporation of protons into the passive film [41,42]. Therefore, it can be identified as a reason for the relatively wide passive range exhibited by

the as-cast HEA-Ta alloy, as depicted in Fig. 4. The Al2s spectra exhibited two peaks at ~ 119 eV and ~ 117 eV, corresponding to oxidic Al^{3+} and metallic Al^0 , respectively. The peak ratio was found to be similar in almost all the alloys with slightly lower intensity for the

metallic Al, except the HEA-Ta (HT) alloy, having most of Al in oxidic form. Co_{2p3/2} spectrum was fitted with three peaks, corresponding to satellite peak, Co_{sat} at ~785 eV (characteristic for Co(II)), oxidic Co²⁺ at ~780 eV and metallic Co⁰ at ~778 eV. The apparently intensive Co⁰ peaks suggested that metallic Co was noticeably present alongside its oxidized form within the passive films. The HEA-Ta (HT) alloy distinctly exhibited low peaks of Co element for both oxidic and metallic forms, suggesting that Co did not contribute to the formation of passive film in this alloy. The Cr_{2p} spectra were deconvoluted by oxidic Cr³⁺ at ~577 eV and metallic Cr⁰ at ~574 eV. All samples displayed similar Cr peaks for both oxidic and metallic states, having much lower intensities for the metallic Cr⁰ peaks than those for the oxidic ones. This indicates that Cr existed in the passive films mainly as oxides rather than its metallic form. The Fe_{2p} spectra were separated into three constituent peaks for the oxidic Fe²⁺ and Fe³⁺ and metallic Fe⁰ at ~713 eV, ~710 eV and ~707 eV, respectively. The oxidic peaks were more intense than those for the metallic state of all the samples. Among the oxidic peaks of Fe, the proportion of the trivalent Fe was larger than the bivalent Fe, which likely corresponds to more pronounced Fe₂O₃ rather than FeOOH [42, 43]. The deconvolution of Ni_{2p} spectra also indicated three peaks, in which two of them, which were found at ~861 eV and ~855 eV, corresponded to other oxidic form of Ni. The metallic Ni⁰ at ~853 eV dominated in the spectra of all the samples, indicating minimal contribution of Ni oxidic species in the passive films. This can be primarily attributed to its lower susceptibility to oxidation in comparison with Fe and Cr, resulting in an enrichment of metallic Ni especially near the surface [44,45]. The Mo_{3d} spectra were split into four peaks, consisting of peaks for Mo⁶⁺ at ~236 eV and ~233 eV and peaks corresponding to metallic Mo⁰ at ~231 eV and ~228 eV. The intensities for both the as-cast and heat-treated HEA-Mo samples were comparable. However, the metallic Mo⁰ peaks were more intensive than those for the oxidic Mo⁶⁺, likely due to its tendency to be enriched in the outer layer of the passive film, which was reported to be beneficial for the formation of stable oxide and improvement of the pitting corrosion resistance [42, 46]. Lastly, the Ta_{4d} peaks were deconvoluted by two peaks, corresponding to oxidic Ta⁵⁺ at ~230 eV, which signified the presence of Ta₂O₅, and metallic Ta⁰ at ~227 eV. The oxidic peaks were more intense than the metallic Ta in both as-cast and heat-treated samples, suggesting that, Ta tended to exist in the passive film in its oxidized form. On the other hand, the as-cast HEA-Ta alloy exhibited much more intense peaks of both Ta⁵⁺ and Ta⁰ than those for the HEA-Ta (HT) alloy, implying that Ta played a significantly more active role in the passive film formed on the surface of the as-cast HEA-Ta alloy.

The fractions of elements contributing to the formation of oxides in passive films are shown in Fig. 8. In general, Al contributed most to the formation of the passive film among the studied elements and existed in the highest fraction as its oxidic form in all the samples. Given that Al is the most reactive component in the studied HEAs, it was expected that it

would oxidize more readily than other elements. This has been consistently reported in numerous studies [43,47,48]. However, the relatively porous nature of the Al oxide film adversely affects the corrosion resistance of the passive film [49]. Among the as-cast alloys, the HEA-Mo alloy displayed the highest fraction of Al oxide within its passive film, while the HEA-Ta alloy had a drastically lower fraction of it compared to the other samples. Following heat treatment, the fraction of Al oxide in the passive films of the HEA-0 and HEA-Mo alloys slightly decreased, while the HEA-Ta (HT) alloy distinctively exhibited far more Al oxide, surpassing all other samples. It is also predictable that the high content of porous Al oxide would increase the oxide film thickness, which may explain the relatively low passive layer resistance (R_1) and the correspondingly high passive film thickness calculated for the HEA-Ta (HT) alloy, as indicated in the EIS results given in Table 3, which was also confirmed by the XPS analyses. The average Co content in the passive films of the alloys was determined to be around 10 ± 2 at.%. Following the heat treatment, the Co oxide ratio in the HEA-0 and HEA-Mo alloys increased, whereas the as-cast HEA-Ta alloy with the highest Co oxide fraction showed a significant decrease after heat treatment, resulting in the lowest Co oxide content among the studied samples. The higher Co content in the oxidic form can result in a significant improvement in the corrosion resistance HEAs, thereby it can be inferred that the contribution of Co oxide to the improvement of the protective capability of the passive layer in the as-cast HEA-Ta alloy was the highest among the studied samples [42,50]. The variation in the fractions of Cr oxide in the passive films of the alloys followed a notable trend resembling that observed for Al oxide, except for the HEA-Mo alloy exhibiting the highest Cr oxide content. It is widely agreed that Cr oxide in the form of Cr₂O₃, is one of the most critical elements contributing to the stability and protective properties of surface films in HEAs. Although Fig. 8 suggests that the as-cast HEA-Mo alloy would exhibit superior passive properties, the CPP test results presented in Fig. 4 and Table 2 showed a low E_{bd} value for this alloy, alongside high i_{corr} and i_{pass} values. This suggests that using high Cr oxide content alone to assess the stability and protectivity of the passive oxide films may not provide a complete or accurate representation. The distribution of different oxides in the passive films of as-cast HEA-Mo and heat-treated HEA-Ta (HT) alloys, which exhibited low passive film stabilities according to CPP and EIS tests, appeared to be notably similar. For example, both alloys showed the highest Al and Cr oxide fractions among the studied samples, while exhibiting the lowest fractions of Co, Fe and Ni based oxides. Although Fe does not significantly affect the passive film properties, higher Ni concentrations mostly gave rise to enhancements in the corrosion performance of various alloys [5,51]. Furthermore, Al₂O₃ and Cr₂O₃ can form a solid solution, which is expected to modify the oxide chemistry and its protective properties [52]. Thus, it can be concluded that especially the high amount of porous Al oxide present in the passive film can have adverse impacts on the corrosion resistance and passivation behaviour.

The relative fractions of metallic and oxidic states of constituent elements in the passive film of HEAs are presented in Fig. 9. It is clear that particularly Al, Co, Cr and Fe were mostly present in the passive films in their oxidic forms in all the alloys. In addition, Ni was found to be mostly in its metallic form in all the alloys, except the HEA-0 (HT) alloy, due to its low migration rate [42]. As mentioned before, Ni generally exhibits high concentrations in regions close to the metal surface, undergoing low oxidation on passive films [45]. The increase in the FCC phase fraction in the HEA-0 (HT) alloy can be considered the primary factor responsible for the higher Ni oxide in the passive film. Mo was also observed to be majorly in its metallic form in the passive films of both as-cast and heat-treated HEA-Mo alloys. It has been reported that Mo was mostly abundant in the outer parts of the passive films whereas it was detected in low amounts in the inner parts [46,53]. Molybdenum significantly increases the pitting corrosion resistance of stainless steels. However, this improvement is primarily due to its enrichment in the outer layer and promotion of stable oxide formation such as Cr₂O₃ rather

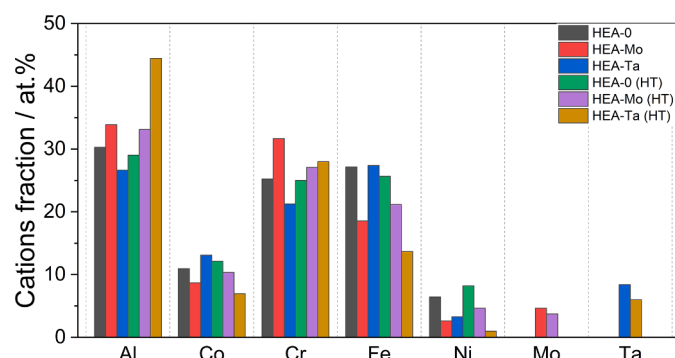


Fig. 8. Fractions of the cationic components in the passive film formed on the as-cast and heat-treated HEAs

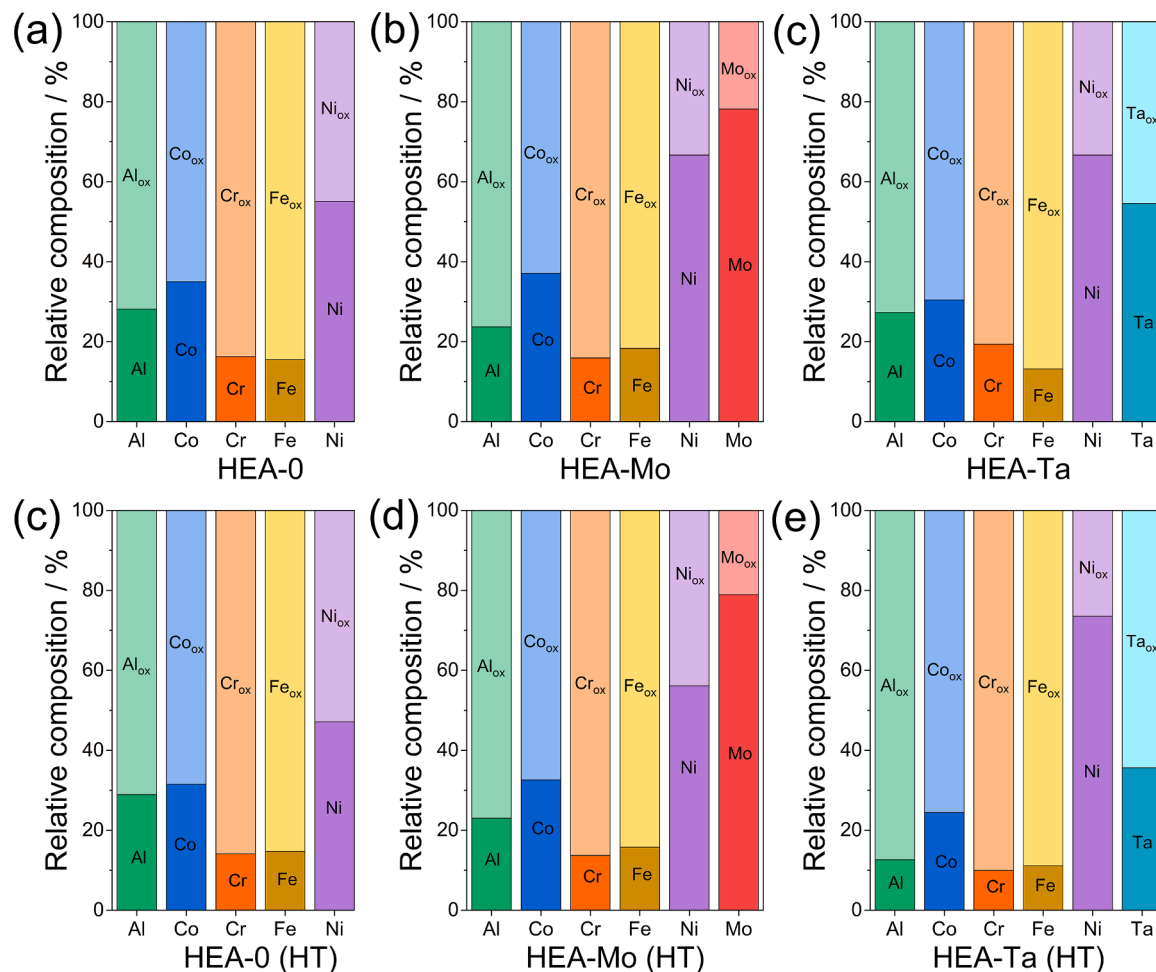


Fig. 9. The relative compositions of metallic and oxidic states of the elements in the passive film of (a) HEA-0, (b) HEA-Mo, (c) HEA-Ta, (d) HEA-0 (HT), (e) HEA-Mo (HT), (f) HEA-Ta (HT)

than the ability of pure Mo to form an effective passive oxide film, which can also explain the high amount of Cr oxide in the HEA-Mo alloy. Ta was mostly present in its metallic form in the passive film of the as-cast HEA-Ta alloy, which was unexpected due to its high oxygen affinity and tendency to form stable Ta₂O₅. However, after the heat treatment process, the fraction of its oxidic form showed an increase, likely due to the presence of larger oxide thickness, having metallic Ta enriched in the inner layer. This could potentially reflect the kinetic limitations during oxide formation or preferential oxidation of other elements with even higher oxygen affinities, such as Al and Cr, in the initial stages of passivation.

4. Conclusion

In this study, the effects of Mo and Ta alloying and heat treatment processes on the corrosion resistance and passivation characteristics of AlCoCrFeNi-based alloys were studied. The key finding can be summarized as follows:

- The microstructure of as-cast base AlCoCrFeNi alloy had fine dendritic morphology, consisting of dendrite core (DR) regions and inter-dendritic (ID) regions, where the primary phase was BCC. The heat treatment promoted the formation of the FCC phase.
- The addition of Mo resulted in the formation of Mo and Cr rich σ phase, whereas Ta addition similarly led to the formation of Ta and Cr rich Laves phase, alongside BCC phases. The compositions of the σ

and Laves phases were slightly enriched in Mo and Ta, respectively, together with Cr, following heat treatment.

- The additions of Mo and Ta significantly improved the hardness of AlCoCrFeNi alloy, with HEA-Ta exhibiting the highest values.
- The CPP curves displayed positive hysteresis confirming pitting corrosion in all the alloys, with limited repassivation. Heat treatment improved repassivation for HEA-0 and HEA-Mo due to the microstructural changes, particularly increased FCC phase in the HEA-0 and the synergistic effects of Mo and Cr in the HEA-Mo alloy.
- HEA-Ta improved pitting resistance but suffered higher corrosion rates after heat treatment due to the increased amount of porous Al oxide and higher possibility of microgalvanic interactions.

CRediT authorship contribution statement

Hüseyin Zengin: Writing – review & editing, Writing – original draft, Visualization, Validation, Resources, Methodology, Investigation, Formal analysis, Data curation, Conceptualization. **Andreas Greul:** Writing – original draft, Validation, Methodology, Investigation, Conceptualization. **Muhammet Emre Turan:** Writing – review & editing, Resources, Methodology, Investigation, Data curation. **Jiri Duchoslav:** Writing – review & editing, Validation, Investigation, Data curation. **Andrei Ionut Mardare:** Writing – review & editing, Validation, Resources, Methodology. **Achim Walter Hassel:** Writing – review & editing, Validation, Supervision, Resources, Methodology, Formal analysis.

Declaration of competing interest

The authors declare that they have no known competing financial interests or personal relationships that could have appeared to influence the work reported in this paper.

Acknowledgements

The authors would like to acknowledge Mr. Michael Pichler for the technical support. J.D. gratefully acknowledges the government of Upper Austria for financial support within the project “ASAES”.

Data availability

No data was used for the research described in the article.

References

- [1] J.-W. Yeh, S.-K. Chen, S.-J. Lin, J.-Y. Gan, T.-S. Chin, T.-T. Shun, C.-H. Tsau, S.-Y. Chang, Nanostructured high-entropy alloys with multiple principal elements: novel alloy design concepts and outcomes, *Adv. Eng. Mater.* 6 (2004) 299–303, <https://doi.org/10.1002/adem.200300567>.
- [2] H. Sahin, H. Zengin, Microstructure, mechanical and wear properties of low-density cast medium and high entropy aluminium alloys, *Int. J. Met.* 16 (2022) 1976–1984, <https://doi.org/10.1007/s40962-021-00744-y>.
- [3] M. Tokarewicz, M. Grądzka-Dahlke, Review of recent research on AlCoCrFeNi high-entropy alloy, *Metals* 11 (2021) 1302, <https://doi.org/10.3390/met11081302>.
- [4] X.-H. Gu, Q.-Y. Huang, J.-B. Chen, H.-S. Hu, Q.-Q. Sun, L.-K. Wu, F.-H. Cao, Optimizing corrosion resistance of equiatomic AlCoCrFeNi high entropy alloys via heat treatment, *J. Alloys Compd.* 968 (2023) 172091, <https://doi.org/10.1016/j.jallcom.2023.172091>.
- [5] A.M. Zemanate, A.M. Jorge Júnior, G.F. de L. Andreani, V. Roche, K.R. Cardoso, Corrosion behavior of AlCoCrFeNix high entropy alloys, *Electrochimica Acta* 441 (2023) 141844, <https://doi.org/10.1016/j.electacta.2023.141844>.
- [6] H. Ren, R.R. Chen, X.F. Gao, T. Liu, G. Qin, S.P. Wu, J.J. Guo, High-performance AlCoCrFeNi high entropy alloy with marine application perspective, *J. Mater. Res. Technol.* 25 (2023) 6751–6763, <https://doi.org/10.1016/j.jmrt.2023.07.135>.
- [7] S. Arun, N. Radhika, B. Saleh, Effect of additional alloying elements on microstructure and properties of AlCoCrFeNi high entropy alloy system: a comprehensive review, *Met. Mater. Int.* (2024), <https://doi.org/10.1007/s12540-024-01752-3>.
- [8] S. Gambaro, L. Fenocchio, F. Valenza, P. Riani, G. Cacciamani, Combined experimental and CALPHAD investigation of equimolar AlCoCrFeNiX ($X=Mo,Ta,W$) high-entropy alloys, *Calphad* 85 (2024) 102702, <https://doi.org/10.1016/j.calphad.2024.102702>.
- [9] A.I. Mardare, C.C. Mardare, J.P. Kollender, S. Huber, A.W. Hassel, Basic properties mapping of anodic oxides in the hafnium–niobium–tantalum ternary system, *Sci. Technol. Adv. Mater.* 19 (2018) 554–568, <https://doi.org/10.1080/14686996.2018.1498703>.
- [10] S.A. Lone, D. Xu, R.B. Cook, A.W. Hassel, Effect of chromium and molybdenum increment on the crystal structure, nanoindentation, and corrosion properties of cobalt-based alloys, *Phys. Status Solidi A* 219 (2022) 2200373, <https://doi.org/10.1002/pssa.202200373>.
- [11] X.-Y. Tian, H.-L. Zhang, Z.-S. Nong, X. Cui, Z.-H. Gu, T. Liu, H.-M. Li, E. Arzikulov, Effect of alloying on microstructure and mechanical properties of AlCoCrFeNi_{2.1} eutectic high-entropy alloy, *Materials* 17 (2024) 4471, <https://doi.org/10.3390/ma17184471>.
- [12] Q. Tian, G. Zhang, K. Yin, W. Wang, W. Cheng, Y. Wang, The strengthening effects of relatively lightweight AlCoCrFeNi high entropy alloy, *Mater. Charact.* 151 (2019) 302–309, <https://doi.org/10.1016/j.matchar.2019.03.006>.
- [13] J. Chen, P. Niu, Y. Liu, Y. Lu, X. Wang, Y. Peng, J. Liu, Effect of Zr content on microstructure and mechanical properties of AlCoCrFeNi high entropy alloy, *Mater. Des.* 94 (2016) 39–44, <https://doi.org/10.1016/j.matdes.2016.01.033>.
- [14] L. Meshi, Y. Linden, A. Munitz, S. Salhov, M. Pinkas, Retardation of the σ phase formation in the AlCoCrFeNi multi-component alloy, *Mater. Charact.* 148 (2019) 171–177, <https://doi.org/10.1016/j.matchar.2018.12.010>.
- [15] J.M. Zhu, H.M. Fu, H.F. Zhang, A.M. Wang, H. Li, Z.Q. Hu, Microstructures and compressive properties of multicomponent AlCoCrFeNiMox alloys, *Mater. Sci. Eng. A* 527 (2010) 6975–6979, <https://doi.org/10.1016/j.msea.2010.07.028>.
- [16] H. Ren, R.R. Chen, X.F. Gao, T. Liu, G. Qin, S.P. Wu, J.J. Guo, Tailoring the microstructure and mechanical properties of Ta-Alloyed AlCoCrFeNi high-entropy alloys, *Metall. Mater. Trans. A* 55 (2024) 2922–2931, <https://doi.org/10.1007/s11661-024-07448-y>.
- [17] F. Ge, H. Yuan, Q. Gao, T. Peng, S. Guo, P. Lyu, Q. Guan, H. Liu, X. Liu, J. Guan, Microstructure, hardness and wear resistance of AlCoCrFeNiTax ($x = 0, 0.1, 0.3$) high-entropy alloys enhanced by laser remelting and Ta addition, *J. Alloys Compd.* 949 (2023) 169741, <https://doi.org/10.1016/j.jallcom.2023.169741>.
- [18] X. Zhang, L. Liu, K. Yao, K. Duan, F. Wu, R. Zhao, Y. Zhang, J. Shang, M. Chen, The phase composition characteristics of AlCoCrFeNi high entropy alloy heat-treated by simple normalizing treatment and its effects on mechanical properties, *J. Alloys Compd.* 926 (2022) 166896, <https://doi.org/10.1016/j.jallcom.2022.166896>.
- [19] W. Guo, J. Li, M. Qi, Y. Xu, H.R. Ezatpour, Effects of heat treatment on the microstructure, mechanical properties and corrosion resistance of AlCoCrFeNiTi0.5 high-entropy alloy, *J. Alloys Compd.* 884 (2021) 161026, <https://doi.org/10.1016/j.jallcom.2021.161026>.
- [20] W.-R. Wang, W.-L. Wang, S.-C. Wang, Y.-C. Tsai, C.-H. Lai, J.-W. Yeh, Effects of Al addition on the microstructure and mechanical property of AlxCrFeNi high-entropy alloys, *Intermetallics* 26 (2012) 44–51, <https://doi.org/10.1016/j.intermet.2012.03.005>.
- [21] J. Han, H. Zhang, H. Yuan, X. Zhuo, X. Cai, Y. Qiao, Effect of heat treatment on the microstructure and corrosion resistance of Al0.75CoCr1.25FeNi high-entropy alloys, *Metals* 14 (2024) 1010, <https://doi.org/10.3390/met14091010>.
- [22] W.S. Tait, An introduction to electrochemical corrosion testing for practicing engineers and scientists: corrosion science, n.d.
- [23] J.D. Henderson, X. Li, F.P. Filice, D. Zagidulin, M.C. Biesinger, B. Kobe, D. W. Shoesmith, K. Ogle, J.J. Noël, Investigating the role of mo and cr during the activation and passivation of Ni-based alloys in acidic chloride solution, *J. Electrochem. Soc.* 168 (2021) 021509, <https://doi.org/10.1149/1945-7111/abe47a>.
- [24] S.B. Inman, J. Han, M.A. Wischhusen, J. Qi, S.R. Agnew, K. Ogle, J.R. Scully, Passivation and localized corrosion resistance of Al0.3Cr0.5Fe2MoxNi1.5Ti0.3 compositionally complex alloys: effect of Mo content, *Corros. Sci.* 227 (2024) 111692, <https://doi.org/10.1016/j.corsci.2023.111692>.
- [25] K. Wang, Y. Zhu, P. Wang, X. Li, B. Malomo, L. Yang, Enhancing corrosion resistance in CoCrFeNiTa high entropy alloys via Mo addition, *Electrochimica Acta* 480 (2024) 143951, <https://doi.org/10.1016/j.electacta.2024.143951>.
- [26] N. Ebrahimi, M.C. Biesinger, D.W. Shoesmith, J.J. Noël, The influence of chromium and molybdenum on the repassivation of nickel-chromium-molybdenum alloys in saline solutions, *Surf. Interface Anal.* 49 (2017) 1359–1365, <https://doi.org/10.1002/sia.6254>.
- [27] Y. Shi, B. Yang, X. Xie, J. Brecht, K.A. Dahmen, P.K. Liaw, Corrosion of AlxCoCrFeNi high-entropy alloys: al-content and potential scan-rate dependent pitting behavior, *Corros. Sci.* 119 (2017) 33–45, <https://doi.org/10.1016/j.corsci.2017.02.019>.
- [28] Z.J. Shi, Z.B. Wang, X.D. Wang, S. Zhang, Y.G. Zheng, Effect of thermally induced B2 phase on the corrosion behavior of an Al0.3CoCrFeNi high entropy alloy, *J. Alloys Compd.* 903 (2022) 163886, <https://doi.org/10.1016/j.jallcom.2022.163886>.
- [29] X.-L. Shang, Z.-J. Wang, Q.-F. Wu, J.-C. Wang, J.-J. Li, J.-K. Yu, Effect of Mo addition on corrosion behavior of high-entropy Alloys CoCrFeNiMox in aqueous environments, *Acta Metall. Sin. Engl. Lett.* 32 (2019) 41–51, <https://doi.org/10.1007/s40195-018-0812-7>.
- [30] A.A. Rodriguez, J.H. Tylickzak, M.C. Gao, P.D. Jablonski, M. Detrois, M. Ziomek-Moroz, J.A. Hawk, Effect of molybdenum on the corrosion behavior of high-entropy alloys CoCrFeNi₂ and CoCrFeNi₂ Mo_{0.25} under sodium chloride aqueous conditions, *Adv. Mater. Sci. Eng.* 2018 (2018) 3016304, <https://doi.org/10.1155/2018/3016304>.
- [31] Y.L. Chou, J.W. Yeh, H.C. Shih, The effect of molybdenum on the corrosion behaviour of the high-entropy alloys Co1.5CrFeNi1.5Ti0.5Mox in aqueous environments, *Corros. Sci.* 52 (2010) 2571–2581, <https://doi.org/10.1016/j.corsci.2010.04.004>.
- [32] C.R. Clayton, Y.C. Lu, A bipolar model of the passivity of stainless steel: the role of Mo addition, *J. Electrochem. Soc.* 133 (1986) 2465, <https://doi.org/10.1149/1.2108451>.
- [33] C. Dai, T. Zhao, C. Du, Z. Liu, D. Zhang, Effect of molybdenum content on the microstructure and corrosion behavior of FeCoCrNiMox high-entropy alloys, *J. Mater. Sci. Technol.* 46 (2020) 64–73, <https://doi.org/10.1016/j.jmst.2019.10.020>.
- [34] Y. Fu, C. Huang, C. Du, J. Li, C. Dai, H. Luo, Z. Liu, X. Li, Evolution in microstructure, wear, corrosion, and tribocorrosion behavior of Mo-containing high-entropy alloy coatings fabricated by laser cladding, *Corros. Sci.* 191 (2021) 109727, <https://doi.org/10.1016/j.corsci.2021.109727>.
- [35] L. Liu, Y. Li, F. Wang, Influence of micro-structure on corrosion behavior of a Ni-based superalloy in 3.5 % NaCl, *Electrochimica Acta* 52 (2007) 7193–7202, <https://doi.org/10.1016/j.electacta.2007.05.043>.
- [36] M.E. Orazem, I. Frateur, B. Tribollet, V. Vivier, S. Marcellin, N. Pébere, A.L. Bunge, E.A. White, D.P. Riener, M. Musiani, Dielectric properties of materials showing constant-phase-element (CPE) impedance response, *J. Electrochem. Soc.* 160 (2013) C215–C225, <https://doi.org/10.1149/2.033061jes>.
- [37] B. Hirschorn, M.E. Orazem, B. Tribollet, V. Vivier, I. Frateur, M. Musiani, Constant-Phase-Element behavior caused by resistivity distributions in films: II. applications, *J. Electrochem. Soc.* 157 (2010) C458, <https://doi.org/10.1149/1.3499565>.
- [38] B. Hirschorn, M.E. Orazem, B. Tribollet, V. Vivier, I. Frateur, M. Musiani, Determination of effective capacitance and film thickness from constant-phase-element parameters, *Electrochimica Acta* 55 (2010) 6218–6227, <https://doi.org/10.1016/j.electacta.2009.10.065>.
- [39] Z. Wang, J. Jin, G.-H. Zhang, X.-H. Fan, L. Zhang, Effect of temperature on the passive film structure and corrosion performance of CoCrFeMoNi high-entropy alloy, *Corros. Sci.* 208 (2022) 110661, <https://doi.org/10.1016/j.corsci.2022.110661>.
- [40] S. Lv, K. Li, Semicconducting behaviour and corrosion resistance of passive film on corrosion-resistant steel rebars, *Materials* 15 (2022) 7644, <https://doi.org/10.3390/ma15217644>.
- [41] S.-I. Pyun, C. Lim, R.A. Oriani, The role of hydrogen in the pitting of passivating films on pure iron, *Corros. Sci.* 33 (1992) 437–444, [https://doi.org/10.1016/0010-938X\(92\)90072-B](https://doi.org/10.1016/0010-938X(92)90072-B).

- [42] Z. Wang, G.-H. Zhang, X.-H. Fan, J. Jin, L. Zhang, Y.-X. Du, Corrosion behavior and surface characterization of an equiatomic CoCrFeMoNi high-entropy alloy under various pH conditions, *J. Alloys Compd.* 900 (2022) 163432, <https://doi.org/10.1016/j.jallcom.2021.163432>.
- [43] Q. Zhao, Z. Pan, X. Wang, H. Luo, Y. Liu, X. Li, Corrosion and passive behavior of AlxCrFeNi_{3-x} ($x = 0.6, 0.8, 1.0$) eutectic high entropy alloys in chloride environment, *Corros. Sci.* 208 (2022) 110666, <https://doi.org/10.1016/j.corsci.2022.110666>.
- [44] C.-O.A. Olsson, D. Landolt, Passive films on stainless steels—chemistry, structure and growth, *Electrochimica Acta* 48 (2003) 1093–1104, [https://doi.org/10.1016/S0013-4686\(02\)00841-1](https://doi.org/10.1016/S0013-4686(02)00841-1).
- [45] E. Hamada, K. Yamada, M. Nagoshi, N. Makiishi, K. Sato, T. Ishii, K. Fukuda, S. Ishikawa, T. Ujiro, Direct imaging of native passive film on stainless steel by aberration corrected STEM, *Corros. Sci.* 52 (2010) 3851–3854, <https://doi.org/10.1016/j.corsci.2010.08.025>.
- [46] M. Uemura, T. Yamamoto, K. Fushimi, Y. Aoki, K. Shimizu, H. Habazaki, Depth profile analysis of thin passive films on stainless steel by glow discharge optical emission spectroscopy, *Corros. Sci.* 51 (2009) 1554–1559, <https://doi.org/10.1016/j.corsci.2008.11.017>.
- [47] Y. Qiu, S. Thomas, D. Fabijanic, A.J. Barlow, H.L. Fraser, N. Birbilis, Microstructural evolution, electrochemical and corrosion properties of AlxCrFeNiTi high entropy alloys, *Mater. Des.* 170 (2019) 107698, <https://doi.org/10.1016/j.matdes.2019.107698>.
- [48] A. Tanji, R. Feng, Z. Lyu, R. Sakidja, P.K. Liaw, H. Hermawan, Passivity of AlCrFeMnTi and AlCrFeCoNi high-entropy alloys in Hanks' solution, *Corros. Sci.* 210 (2023) 110828, <https://doi.org/10.1016/j.corsci.2022.110828>.
- [49] Y.-F. Kao, T.-D. Lee, S.-K. Chen, Y.-S. Chang, Electrochemical passive properties of AlxCrFeNi ($x = 0, 0.25, 0.50, 1.00$) alloys in sulfuric acids, *Corros. Sci.* 52 (2010) 1026–1034, <https://doi.org/10.1016/j.corsci.2009.11.028>.
- [50] X. Qiu, M. Wu, C. Liu, Y. Zhang, C. Huang, Corrosion performance of Al₂Cr₂Fe₃Cu₂Ni₂Ti high-entropy alloy coatings in acid liquids, *J. Alloys Compd.* 708 (2017) 353–357, <https://doi.org/10.1016/j.jallcom.2017.03.054>.
- [51] C.M. Abreu, M.J. Cristóbal, R. Losada, X.R. Nóbrega, G. Pena, M.C. Pérez, The effect of Ni in the electrochemical properties of oxide layers grown on stainless steels, *Electrochimica Acta* 51 (2006) 2991–3000, <https://doi.org/10.1016/j.electacta.2005.08.033>.
- [52] P. Zhao, H. Zhao, J. Yu, H. Zhang, H. Gao, Q. Chen, Crystal structure and properties of Al₂O₃–Cr₂O₃ solid solutions with different Cr₂O₃ contents, *Ceram. Int.* 44 (2018) 1356–1361, <https://doi.org/10.1016/j.ceramint.2017.08.195>.
- [53] Z. Wang, Z. Feng, L. Zhang, Effect of high temperature on the corrosion behavior and passive film composition of 316 L stainless steel in high H₂S-containing environments, *Corros. Sci.* 174 (2020) 108844, <https://doi.org/10.1016/j.corsci.2020.108844>.